Int J Adv Manuf Technol (2017) 91:771–780
DOI 10.1007/s00170-016-9806-7

ORIGINAL ARTICLE

Investigation of welding parameters on microstructure and mechanical properties of laser beam-welded joint of 2060 Al–Cu–Li alloy

Cheng Gu[1] · Yanhong Wei[1] · Xiaohong Zhan[1] · Dan Zhang[1] · Shuai Ren[1] · Hongbing Liu[2] · Hao Li[2]

Received: 17 September 2016 / Accepted: 21 November 2016 / Published online: 28 November 2016

Abstract 2060 Al–Cu–Li alloy plates with 2- and 1-mm thickness were welded by a fiber laser beam. The weld microstructure features and the mechanical properties such as microhardness and tensile strength of 2060 Al–Cu–Li alloy laser beam-welded joint were investigated to study the influence of welding parameters on the weld bead. By microstructure and mechanical property analysis, it is found that weld width as well as penetration depth increases with the increase of laser power when the welding speed is constant. The microstructures of the fusion line and fusion zone show similar dendrite morphologies with traditional cast structure under the thermal cycling. Fine grain zone can be observed near the fusion line. Welding porosities exist in the microstructure of 2060 Al–Cu–Li laser beam-welded joint. Porosity ratio increases at first, and then declines, and then increases again with the increase of laser power. The larger heat input causes the lower microhardness distribution of the corresponding joint. The optimized welding parameters of fiber laser beam welding of 2- and 1-mm-thick 2060 Al–Cu–Li alloys are 2500 W and 3 m/min and 2300 W and 4 m/min, respectively.

Keywords Laser beam welding · 2060 Al–Cu–Li alloy · Microstructure · Mechanical property

✉ Xiaohong Zhan
xiaohongzhan_nuaa@126.com

[1] College of Material Science and Technology, Nanjing University of Aeronautics and Astronautics, Nanjing 211106, China

[2] Shanghai Aircraft Manufacturing Company Limited, Shanghai 200436, China

1 Introduction

Aluminum alloy is a kind of potential materials for lightweight constructions especially in the aeronautical and automotive industry due to the good mechanical properties and low density [1]. Laser beam welding (LBW) has been used as an appropriate joining technology for Al alloy due to many advantages including slight heat damage to base material, good weld appearance, perfect quality, little amount of deformation of welded joint, etc. Thus, LBW of Al alloy is of considerable interest and desirable for lightweight structural applications.

Many studies on LBW of Al alloy have been performed recently [2–6]. Ancona et al. [7] provided a quantitative study on the laser weldability of AA5083 Al–Mg alloy specimens in butt joint configuration. They found that best performances could be obtained by operating at 2500 W and 100 mm/s where it was found a tensile strength of more than 90% with respect to the native material, a porosity level less than 3%, and just a small hardening across the weld zone. Yang et al. [8] have fabricated T-joints consisting of 1.8-mm-thick AA6156-T6/AA6056-T4 Al alloys by double-sided LBW using a eutectic alloy AA4047 filler wire. Efforts have been made to find that crack-free welds with minor porosity could be obtained by careful surface preparation, usage of suitable filler materials, and optimization of processing parameters. Gao et al. [9] carried out laser–cold metal transfer arc hybrid welding of 6061 Al alloy and AISI304 stainless steel (304SS). The optimal parameter ranges for accepted bead appearances were obtained, which are laser power 1.8–2.1 kW, wire filling rate 4.8–5.4 m/min, laser offset 0.4–0.8 mm, and welding speed 2–3 m/min.

Nowadays, the pressure for higher strength and improved fracture toughness with reduced weight in aircraft applications have resulted in the development of new generation of Al–Li

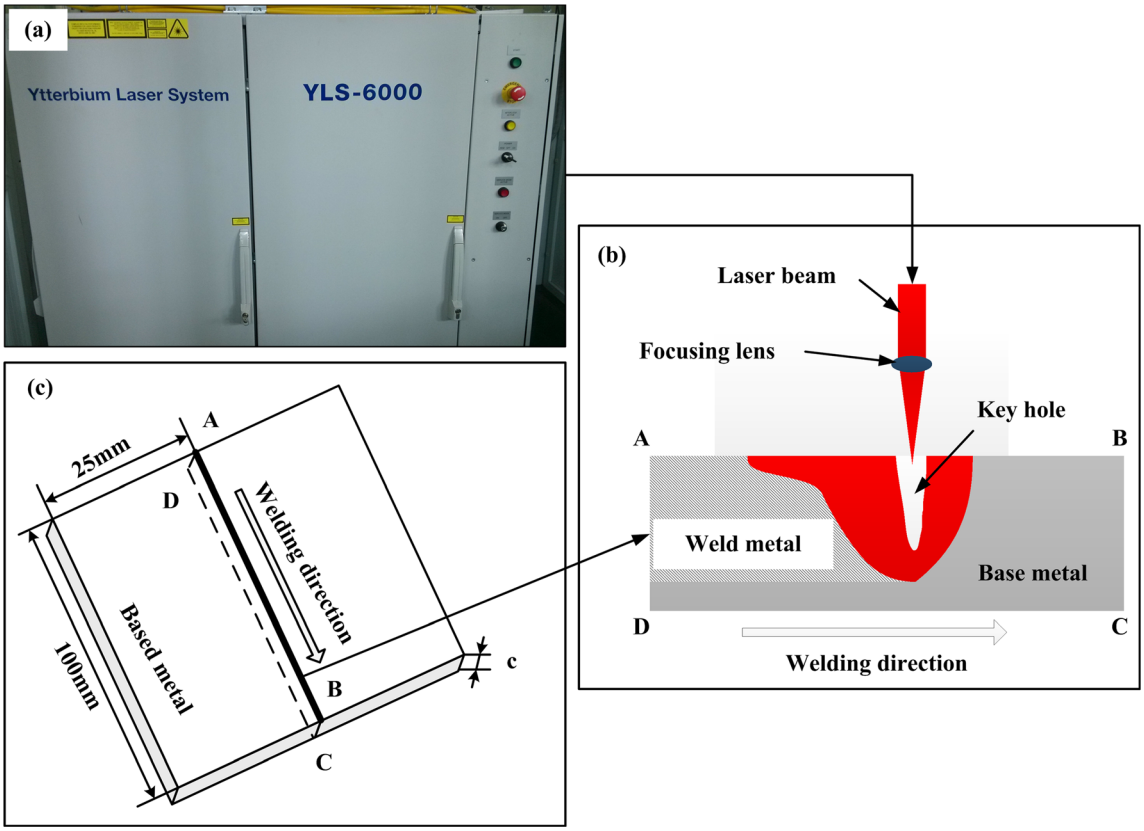

Fig. 1 Welding system including **a** laser device, **b** schematic illustration for the workpiece, and **c** welding plates

alloys [10]. Molian et al. [11] evaluated the weldability characteristics of the A1–2.7Cu–2.2Li–0.12Zr alloy 2090 joined by a high-energy-density source in comparison with conventional fusion welding processes. Weld depth (penetration) and weld width decreased exponentially, with a decrease in traverse speed of the laser beam, indicating a transition in the mechanism from deep penetration to conduction weld. And only few pores were observed on the weld/base material interface, and the degree of porosity of the laser weld was observed to be unaffected by the depth of penetration. Hou et al. [12] investigated the effect of solute segregation on the weld fusion zone microstructure in CO_2 laser beam (LB) and gas tungsten arc (GTA) welds in 2195 Al–Li alloy. Solidification segregation and the associated depletion of alloying elements in the dendrite cores resulted in negligible precipitation in these regions. Shi et al. [13] investigated the effect of laser welding on the tear toughness and microstructure of a commercial 1420 Al–Li alloy sheet. Their test results indicate that the tear energies or tear toughness has slight orientation dependence for the 1420 Al–Li alloy thin sheet. Fu et al. [14] tested the LBW ability of 2A97 Al–Li alloy and discussed the microstructure evolution mechanism and its relationship with mechanical properties through the investigation of weld appearance, microstructure, element segregation, precipitate distribution, and the mechanical properties of welded joints. Yan et al. [15] investigated the microstructure and mechanical properties of 1420 Al–Li alloy joints before and after heat treatment by CO_2 laser–metal inter gas (MIG) hybrid welding. The tensile strengths of joints before and after heat treatment were 223 and 267 MPa, reaching up to 57 and 68% of the parent materials' strength, respectively.

However, most of the researches mainly focused on previous Al–Li alloys over the past two decades. There are few reports on LBW of the newly developed 2060 Al–Cu–Li alloy, which is characterized by excellent properties of antifatigue crack growth and corrosion resistance and improved ductility and toughness [16]. Zhang et al. [17] investigated the weld microstructure features and the resultant joint mechanical properties of 2060 Al–Cu–Li alloy in LBW with an addition of Mg-rich filler metal, while there is no systematical investigation on parameter optimization, microstructure characterization, and

Table 1 The composition of 2060-T8 Al–Cu–Li alloy (wt%)

	Cu	Li	Mg	Zn	Mn	Zr	Ag	Si	Fe	Ti	Al
2060-T8	3.9	0.80	0.70	0.32	0.29	0.1	0.34	0.02	0.02	<0.10	Balanced

Table 2 Parameters used in welding experiments

Case	Plate thickness (mm)	Laser power (W)	Welding speed (m/min)	Heat input (kJ/m)
1	2	1800	3	36
2	2	2000	3	40
3	2	2300	3	46
4	2	2500	3	50
5	2	2800	3	56
6	1	1800	4	27
7	1	2000	4	30
8	1	2300	4	34.5
9	1	2500	4	37.5
10	1	2800	4	42

mechanical properties of the laser-welded 2060 Al–Cu–Li alloy till now. In this study, investigation on 2- and 1-mm-thick 2060 Al–Cu–Li alloy plates is performed using high-power fiber laser welding. Surface morphologies, microstructures, mechanical properties, and weld porosities of the weld bead with different parameters are discussed by considering the welding parameters such as laser power, welding speed, and plate thickness. The results of the study can provide foundation for the employment and the improvement of fiber LBW of 2060 Al–Cu–Li alloys in aircraft manufacturing.

2 Experimental procedure

2.1 Equipment setup

An IPG (YLS-6000) laser device and a Kuka (KR 30HA) welding robot are used in this work. The former provides thermal source for laser welding process, and the latter attached by laser device enables simultaneous moving. The welding system is shown in Fig. 1.

2.2 Materials and welding parameters

The chemical composition of 2060-T8 Al–Cu–Li alloy is listed in Table 1. In this study, experiments on fiber laser welding of 2- and 1-mm-thick 2060 Al–Cu–Li plates are performed. Two factors including laser power and welding velocity are considered. Before welding, the samples are polished by an emery paper and cleaned using acetone to remove oil and contamination. Thereafter, the surface is wiped out with alcohol. Argon gas is applied to protect the molten pool using the coaxial back blowing method with the gas flow rate of 15 L/min. The welding parameters used in welding experiments are shown in Table 2. After welding, the workpieces are prepared by wire cut electric discharge machine, of which the cross sections are polished into a mirror-like surface and etched with Keller's solution (95% H_2O + 2.5% HNO_3 + 1.5% HCl + 1.0% HF) for weld bead appearance analysis. Then, the morphology of the welded joint is investigated using a metallographic microscope. A HV1000A microhardness testing machine is used to measure the hardness of the samples. A tensile test is also performed in this

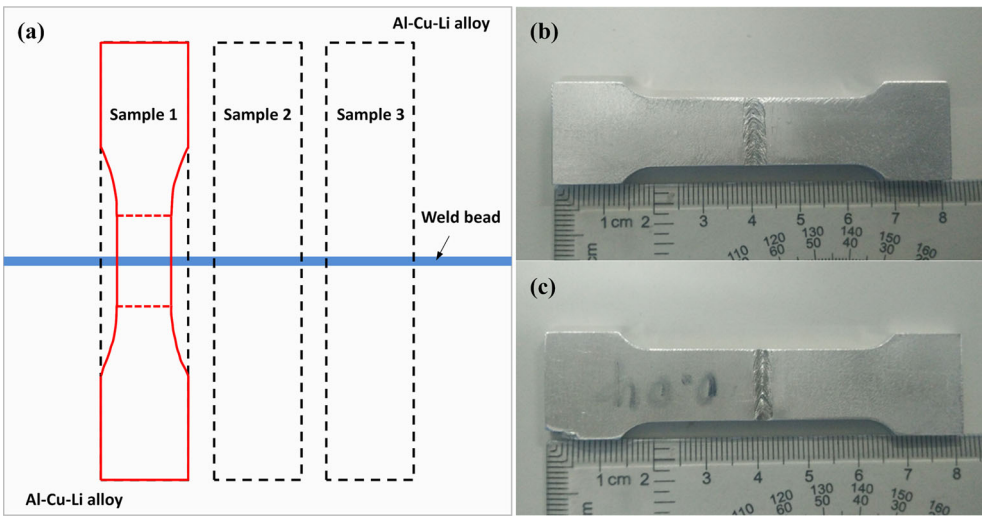

Fig. 2 **a** Diagram of tensile test samples. **b** Morphology of the 2-mm-thick tensile test sample. **c** Morphology of the 1-mm-thick tensile test sample

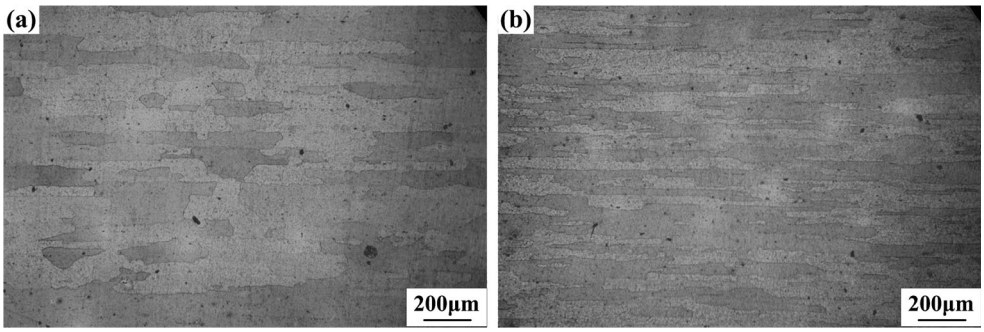

Fig. 3 Optical micrograph of 2060-T8 Al–Li alloy. **a** Longitudinal plane. **b** Transverse plane

study, as tensile property of the welded joints can verify its quality. The tensile samples are cut according to the GB/T228 standard, and a WDW-100 universal testing machine is used to conduct the tensile test. Tensile tests are done for three times. Figure 2 shows the diagram and morphology of the tensile test samples.

3 Results and discussion

The microstructures of the base metal, 2060-T8 Al–Cu–Li alloy, are shown in Fig. 3. It can be seen that the microstructures in the longitudinal plane and the transverse plane of the base metal show highly elongated grains along the rolling direction.

Figure 4 shows the top and bottom surface morphologies and cross sections of the welded joint with different welding parameters. The cross sections of the welded joint clearly show the morphology of the weld bead. It can be observed that the weld width increases as well as the penetration depth with the increase of laser power when the welding speed is constant. At the same time, it shows that the main defect of LBW includes lack of penetration, weld crack, and oxidation (Fig. 4f). A lack of penetration as shown in Fig. 4a occurs in the situation with a small laser power. Weld crack may appear on both inside and outside of the weld bead when the laser power is inappropriate as shown in Fig. 4b. With the increase of the heat input, oxidation problem becomes even serious as shown in Fig. 4f. These welding defects lead to poor welding quality. In other words, moderate heat input leads to high-quality weld bead with full penetration, no cracks, and less oxidation as shown in Fig. 4c, e. Thus, the heat input including the laser power and welding velocity should be controlled within a reasonable range during welding.

Several morphologies and microstructures of the 2- and 1-mm-thick welded joints with different welding parameters are shown in Figs. 5 and 6. As mentioned previously, when the welding velocity is deemed to be a constant value, heat input of the welded joint depends on the laser power. It is believed that with the increase of the heat input, the fusion depth and width of the welded joint increase. It should be noted that the microstructures of the fusion line and fusion zone show

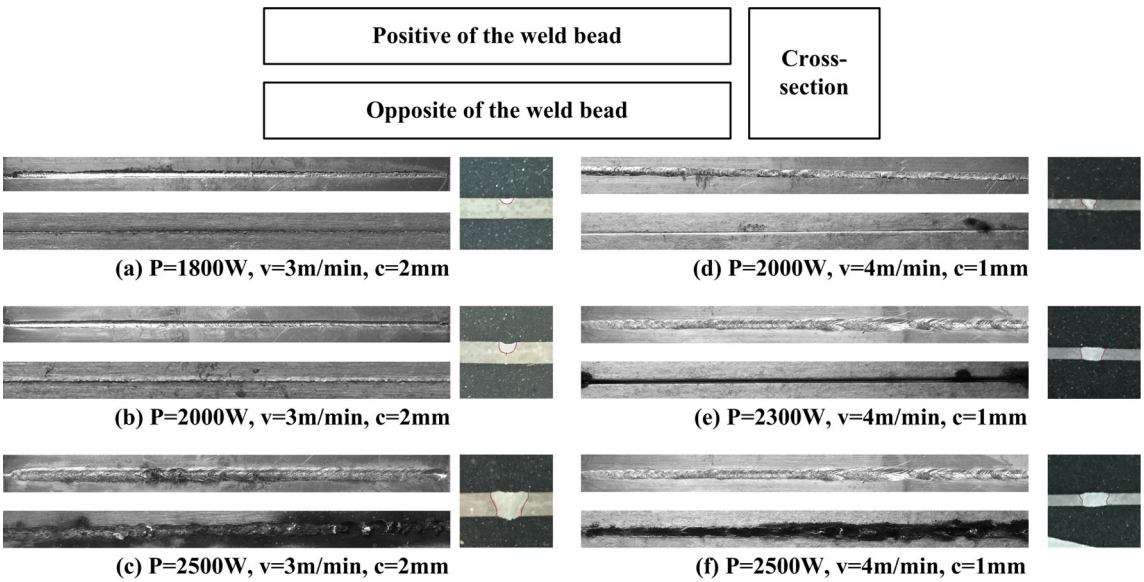

Fig. 4 Surface morphologies and cross sections of the welded joint with welding parameters: **a** P = 1800 W, v = 3 m/min, and c = 2 mm; **b** P = 2000 W, v = 3 m/min, and c = 2 mm; **c** P = 2500 W, v = 3 m/min, and c = 2 mm; **d** P = 2000 W, v = 4 m/min, and c = 1 mm; **e** P = 2300 W, v = 4 m/min, and c = 1 mm; and **f** P = 2500 W, v = 4 m/min, and c = 1 mm

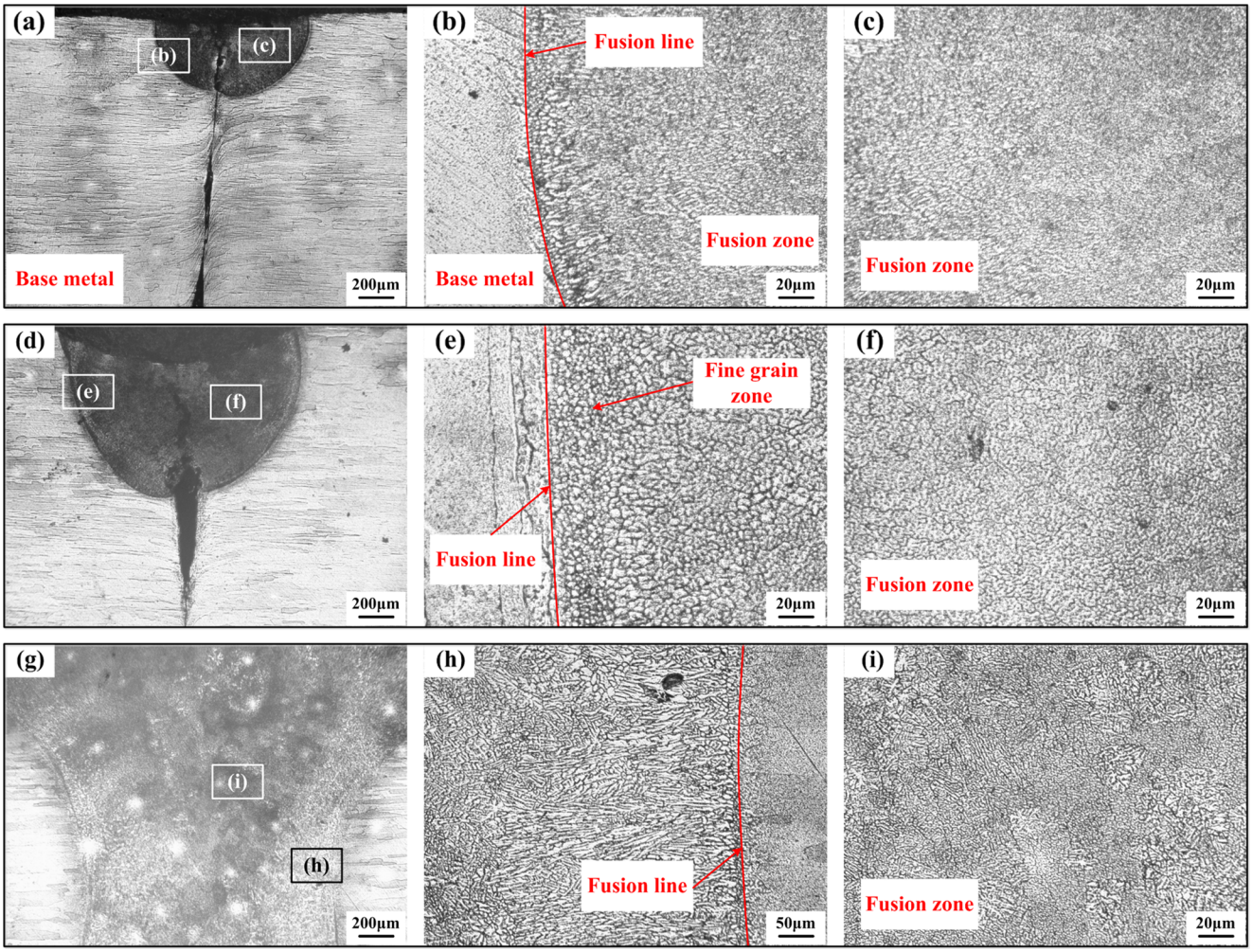

Fig. 5 Morphologies and microstructures of the 2-mm-thick welded joint with different welding parameters: **a** P = 1800 W, v = 3 m/min, and c = 2 mm; **b** fusion line microstructure of weld bead in **a**; **c** fusion zone microstructure of weld bead in **a**; **d** P = 2000 W, v = 3 m/min, and c = 2 mm; **e** fusion line microstructure of weld bead in **d**; **f** fusion zone microstructure of weld bead in **d**; **g** P = 2500 W, v = 3 m/min, and c = 2 mm; **h** fusion line microstructure of weld bead in **g**; and **i** fusion zone microstructure of weld bead in **g**

similar dendrite morphologies with traditional cast structure under the thermal cycling of the welding process. As shown in Fig. 5b, it can be seen that the heat-affected zone is very small due to the large cooling rate. The microstructures in the base metal nearly remain unchanged. Fine grain zone can be observed near the fusion line. The solidification happens at the fine grain zone, which is the typical microstructure of Al–Li alloy. The generation of the fine grain zone is difficult because the time lapsed at high temperature is too short for the nuclei to grow large and coarse, and the diffusion and growth are incomplete. Therefore, newly developed grains maintain small and form the fine grain zone. Then, the columnar dendrites grow from the fine grain zone along the direction of temperature gradient. The columnar dendrites grow outward from the base metal. The number of dendrite reduces, and the dendrite size becomes coarser due to the competitive growth of the dendrites. All the columnar dendrites grow from the base metal to the center on the top surface. That is to say, the growth direction of the columnar dendrite is different from place to place, which is due to the characteristic of LB heat source. With the solidification proceeding, the direction of the temperature gradient is gradually blurred and tends to be uniform. This is the reason why the nucleation and growth of the equiaxed grains happen. From Fig. 5c, it can be seen that equiaxed grains exist in the middle of the weld bead. The microstructure of the LB-welded Al–Cu–Li alloy is relatively different from others [18–21].

Similarly, microstructures can be observed in the 1-mm-thick weld joint. It is found that with weld penetration depths increasing, the area of the fine grain zone increases. It is because that the fusion zone, where the fusion line in the upper part of molten pool is near, stays at high temperature longer than that in the lower part of molten pool due to the characteristic of LBW. In other words, the high temperature and the fast welding speed cause large temperature gradient/crystallization rate (G/R) ratio at the beginning of the

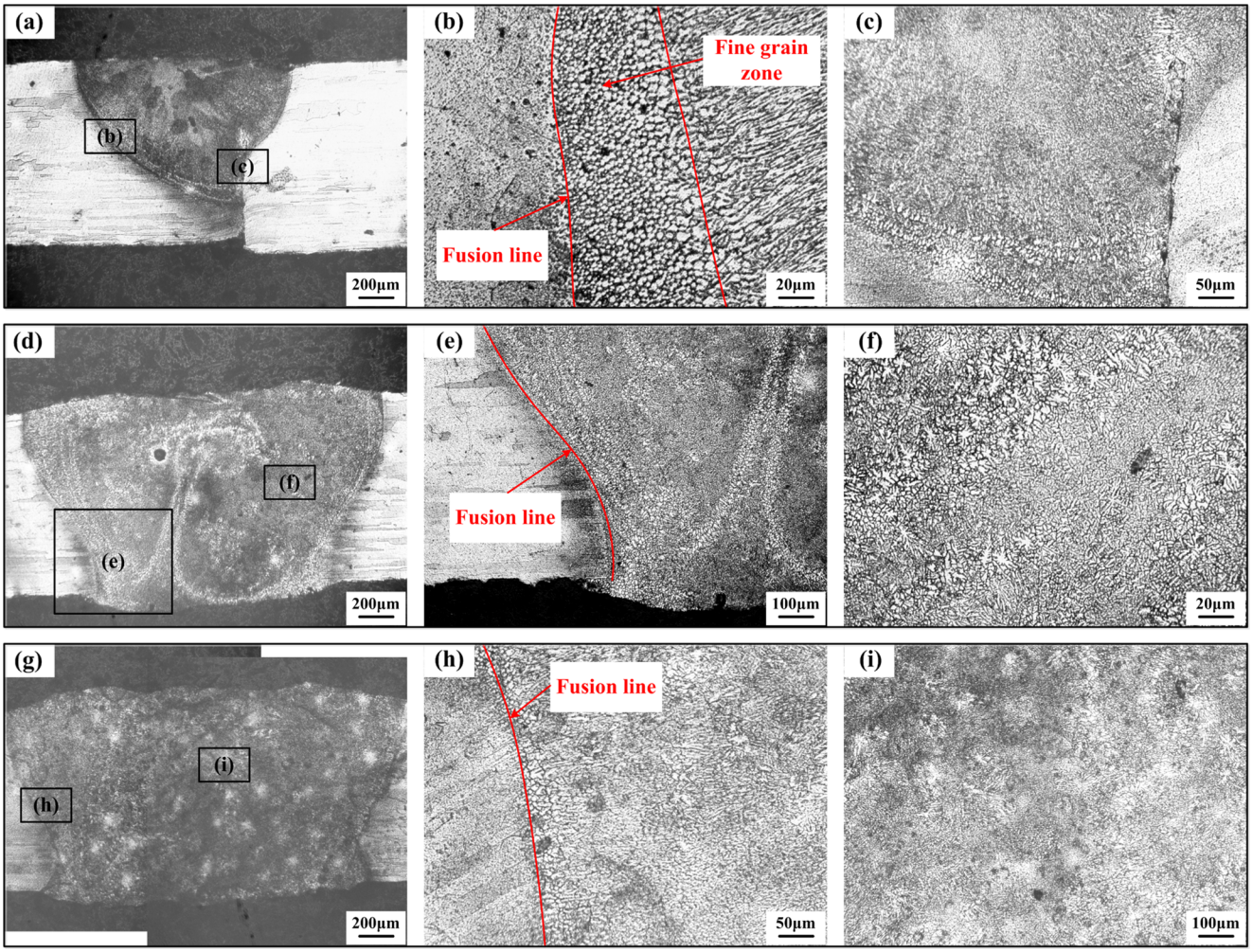

Fig. 6 Morphologies and microstructures of the 1-mm-thick welded joint with different welding parameters: **a** P = 2000 W, v = 4 m/min, and c = 1 mm; **b** fusion line microstructure of weld bead in **a**; **c** fusion zone microstructure of weld bead in **a**; **d** P = 2300 W, v = 4 m/min, and c = 1 mm; **e** fusion line microstructure of weld bead in **d**; **f** fusion zone microstructure of weld bead in **d**; **g** P = 2500 W, v = 4 m/min, and c = 1 mm; **h** fusion line microstructure of weld bead in **g**; and **i** fusion zone microstructure of weld bead in **g**

solidification. Then, at the edge of the molten pool (near the fusion line), it is difficult for nuclei to grow large and coarse. This is also the reason why the fine grain zone appears. It can be seen that a good weld bead is obtained with a laser power of 2000 W and a welding velocity of 4 m/min. When the laser power is 2500 W, the weld bead is burned through, and oxidation problem occurs at the opposite side of the plate. At the same time, it is found that the size of the fine grain zone increases with depth, which is related to the distribution and cycling characteristics of temperature in the molten pool during the fiber laser welding.

Porosity is a kind of common defect in the welding of Al alloy. The occurrence of welding pores will reduce the air tightness of the welded joints. At the same time, it will reduce the weld cross-sectional area, carrying capacity, tensile strength, and fatigue strength of the welded joints. And porosity can induce stress concentration and even cause the generation of cracks. It is believed that there are two kinds of porosities during the LBW of Al alloy: keyhole-induced porosity and metallurgy porosity. Gas bubbles intermittently form from the tip of the oscillating keyhole, and some of them are captured by the solidification front and then become keyhole-induced porosities during the LBW [22]. Hydrogen element is the reason of metallurgy porosity formation during the LBW of Al alloy. The solubility of hydrogen decreases rapidly with the decrease of temperature during the solidification process. The large thermal conduction of Al alloy results in rapid cooling rate of the molten pool. When the escape speed of the hydrogen bubble is smaller than the solidifying speed of the molten pool, hydrogen porosity will form in the weld bead. The morphology of the porosity formed in LB-welded joint of 2060 Al–Cu–Li alloy is shown in Fig. 7.

The porosity ratio in this study is the statistical data of the proportion of porosity in the total cross-sectional area of the weld bead, which is obtained by measuring the three cross sections of the weld bead. The porosity ratio

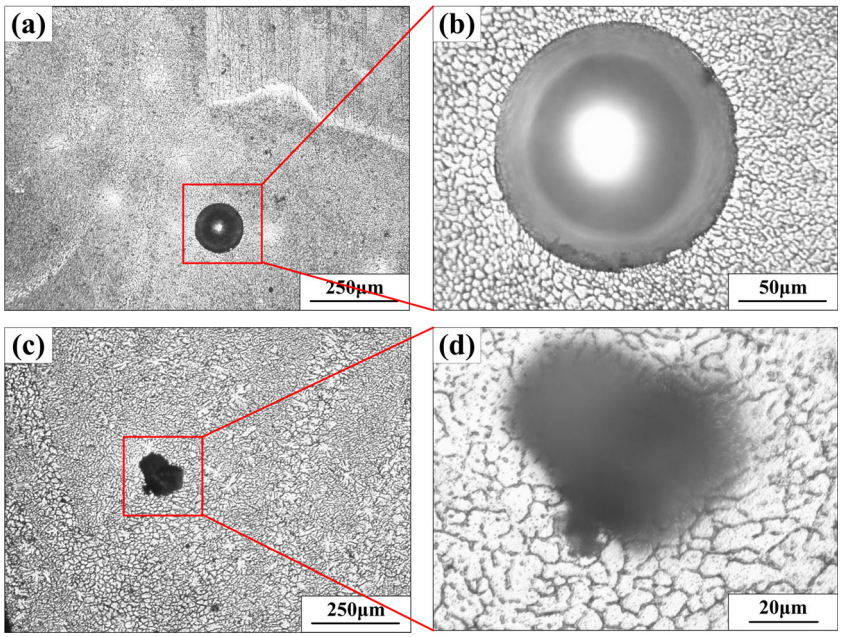

Fig. 7 The morphology of the porosity formed in laser beam welding joint of 2060 Al–Cu–Li alloy

is closely related to the welding parameters, especially the welding power. The porosity information of the 2- and 1-mm-thick weld beads is recorded in Tables 3 and 4. It can be clearly seen that with the increase of heat input, the porosity ratio increases at first, and then declines, and then increases again when welding the 2-mm-thick plates. The porosity ratio of the 1-mm-thick weld bead shows a similar tendency. When the heat input is 27 kJ/m, the porosity ratio of the 1-mm-thick weld bead is relatively low. The reason is that a lack of penetration occurs with a small laser power. And the porosity ratio of the 1-mm-thick weld bead is the lowest when the heat input is 34.5 kJ/m. Thus, few or even no porosity is generated under adequate heat input, while large amount of porosity appears with too high or too low heat input. Moreover, it can be seen that the porosity of the 2-mm-thick weld bead is found to be lower, which opposes the general viewpoint describing that more porosity tends to appear in thicker plate. The reason may lie in that the heat input of the 2-mm sample is larger than that of the 1-mm sample. As a result, the cooling rate is lower, so the bubbles have more time to escape out of the 2-mm-thick sample than that of the 1-mm sample.

Microhardness distribution across the 2-mm-thick 2060 Al–Cu–Li alloy welded joints with different welding parameters is shown in Fig. 8. Microhardness results of the base metal (BM), heat-affected zone (HAZ), and fusion zone (FZ) are recorded. It is clear that the microhardness of BM is the highest and that of HAZ is the lowest. The reason is that the BM of 2060-T8 Al–Cu–Li alloy is strengthened by thermal deformation and aging strengthening treatment as the microstructures shown in Fig. 3. After the welding process, the strengthening effect is decreased since alloying elements in the FZ are burned loss. At the same time, HAZ experiences high-temperature heating without melting. The thermal cycling makes grains in HAZ grow coarse and form a "softening zone." Thus, the microhardness of HAZ decreases. It is interesting that the microhardness of the fine grain zone is high. As shown in Fig. 6b, the grains with micron size form a high microhardness zone. It should be noted that the larger heat

Table 3 Porosity of 2-mm-thick weld bead

No.	Heat input (kJ/m)	Average diameter of porosity (μm)	Number of porosities	Weld cross-sectional area (mm^2)	Average porosity ratio (%)	Standard deviation (%)
1	36	5.86	165	0.348	1.278	0.047
2	40	13.72	75	0.852	1.301	0.065
3	46	10.93	134	1.967	0.639	0.033
4	50	13.16	26	3.903	0.077	0.012
5	56	12.81	134	4.213	0.410	0.016

Table 4 Porosity of 1-mm-thick weld bead

No.	Heat input (kJ/m)	Average diameter of porosity (μm)	Number of porosities	Weld cross-sectional area (mm^2)	Average porosity ratio (%)	Standard deviation (%)
1	27	2.78	151	0.220	0.417	0.012
2	30	20.48	32	0.741	1.422	0.051
3	34.5	13.96	52	1.958	0.406	0.009
4	37.5	12.19	327	2.726	1.400	0.033
5	42	14.52	246	2.834	1.437	0.042

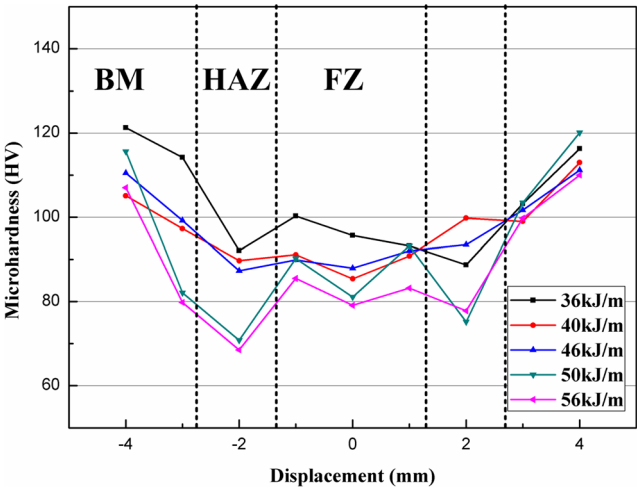

Fig. 8 Microhardness distribution across the 2-mm-thick weld bead using different welding parameters (v = 3 m/min)

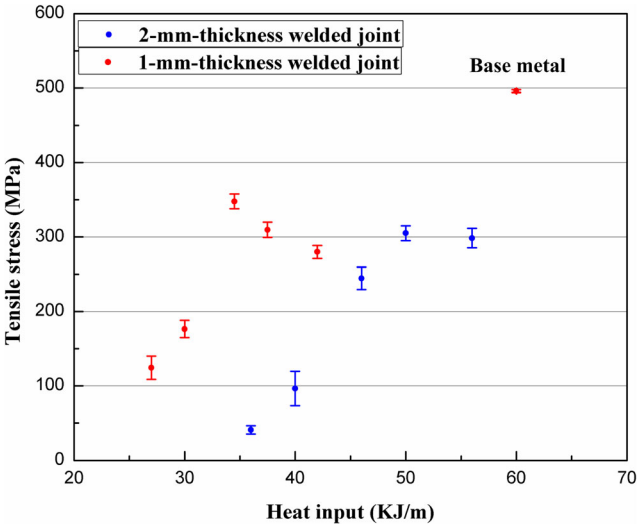

Fig. 9 Tensile test results of welding samples

input causes the lower microhardness distribution of the corresponding joint. When the welding speed is 3 m/min, the average microhardness of the whole welded joint increases with the decrease of the laser power.

The tensile test results are listed in Table 5. The results show that the average ultimate tensile strengths of 2- and 1-mm 2060 Al–Cu–Li alloy plates are 494.6 and 497.5 MPa, respectively. The elongations of 2- and 1-mm 2060 Al–Cu–Li alloy plates are 13.9 and 14.1%, respectively. The mechanical property of the base metal is almost the same with the results of Zhang [17].

Then it can be seen that the tensile strength of the welded joint is much lower than that of the base material, while the relative low strength is due to the brittle fracture that occurred at the weld bead. In the 2-mm-thick 2060 Al–Cu–Li welded joints, when the heat input is 50 kJ/m, the largest tensile strength is 305.0 MPa, about 61.7% of that of the base metal. When the heat input is 36 and 40 kJ/m, it is clearly known from the microstructural analysis in Fig. 5 that a lack of penetration occurs in the weld bead. This defect decreases the weld quality sharply and leads to the low tensile stress and elongation. The average elongation shows a tendency to increase first and then decrease. And the largest average elongation agrees with the largest tensile stress.

In the 1-mm-thick 2060 Al–Cu–Li welded joints, when the heat input is 34.5 kJ/m, the largest tensile strength is 337.8 MPa, about 67.9% of that of the base metal. It should be noted that the average tensile stress of the welded joint using heat input of 37.5 and 42 kJ/m is less than that of 34.5 kJ/m. As mentioned previously, a too large laser power leads to overburn, which decreases the mechanical property of the welded joint.

At the same time, the tensile test results with error bars of 2- and 1-mm 2060 Al–Cu–Li samples are shown in Fig. 9. It should point out that the heat input, which is used to obtain

Table 5 Tensile testing results of 2- and 1-mm-thick 2060 Al–Cu–Li alloy plate

No.	Sample thickness (mm)	Heat input (kJ/m)	Average tensile stress (MPa)	Average elongation (%)	Fracture location
1	2	Base metal	494.6	13.9	Base metal
2	2	56	304.4	7.6	Weld bead
3	2	50	315.0	7.8	Weld bead
4	2	46	254.6	4.9	Weld bead
5	2	40	96.5	1.6	Weld bead
6	2	36	40.7	0.7	Weld bead
7	1	Base metal	497.5	14.1	Base metal
8	1	42	279.9	7.2	Weld bead
9	1	37.5	309.5	7.4	Weld bead
10	1	34.5	347.7	8.1	Weld bead
11	1	30	176.5	1.5	Weld bead
12	1	27	124.4	0.9	Weld bead

the largest tensile stress in the 2-mm-thick 2060 Al–Cu–Li welded joints, is almost twice of the heat input used to obtain the largest tensile stress in 1-mm-thick welded joints. This situation just agrees with that the 2-mm-thick welded joints are twice the 1-mm-thick welded joints. It is evident that the largest tensile strength can be obtained with appropriate heat input. Thus, the importance of heat input on welding quality of 2060 Al–Cu–Li alloy is proved.

4 Conclusions

In this study, high-power fiber laser welding on 2060 Al–Cu–Li alloy plate is performed considering the factors such as plate thick, laser power, and welding speed. The weld microstructure features and the mechanical properties such as microhardness and tensile strength of 2060 Al–Cu–Li alloy LB-welded joint are obtained to study the influence of welding parameters on weld bead.

Weld width as well as penetration depth increases with the increase of laser power when the welding speed is constant. And insufficient welding power can lead to lack of penetration, while excessive welding power can cause other weld defects such as overburn. The microstructures of the fusion line and FZ show similar dendrite morphologies with traditional cast structure under the thermal cycling. The fine grain zone can be observed near the fusion line. With weld penetration depths increasing, the area of fine grain zone increases. The generation of the fine grain zone is difficult because the time lapsed at high temperature is too short for the nuclei to grow large and coarse, and the diffusion and growth are incomplete. The high temperature and the fast welding speed cause large temperature gradient/crystallization rate (G/R) ratio at the beginning of the solidification. Then, at the edge of the molten pool (near the fusion line), it is difficult for nuclei to grow large and coarse.

Welding porosities exist in the microstructure of 2060 Al–Cu–Li LB-welded joint. With the increase of heat input, the porosity ratio increases at first, and then declines, and then increases again when welding the 2-mm-thick plates with 3 m/min. The porosity ratio of the 1-mm-thick weld bead shows a similar tendency. Microhardness of the base metal is the highest, and that of the HAT is the lowest. The larger heat input causes the lower microhardness distribution of the corresponding joint. The ultimate welded joint tensile strengths of the 2- and 1-mm-thick 2060 Al–Cu–Li alloys are 305.0 and 337.8 MPa, about 61.7 and 67.9% of that of the base metal. By microstructure and mechanical property analysis, the optimized welding parameters for the 2- and 1-mm-thick 2060 Al–Cu–Li alloys are 2500 W and 3 m/min and 2300 W and 4 m/min, respectively.

Acknowledgements The authors gratefully acknowledge a Project Funded by the Priority Academic Program Development of Jiangsu Higher Education Institutions (PAPD) and the financial support of the project from the Fundamental Research Funds for the Central Universities NP2016204, the National Natural Science Foundation of China (Grant no. 51175253), and the National Commercial Aircraft Manufacturing Engineering Technology Research Center Innovation Fund of China (SAMC14-JS-15-052).

References

1. Schubert E, Klassen M, Zerner I, Walz C, Sepold G (2001) Lightweight structures produced by laser beam joining for future applications in automobile and aerospace industry. J Mater Process Technol 115(1):2–8
2. Haboudou A, Peyre P, Vannes AB, Peix G (2003) Reduction of porosity content generated during Nd:YAG laser welding of A356 and AA5083 aluminium alloys. Mater Sci Eng A 363(1–2):40–52
3. Wang X, Wang H, Lu F, Carlson BE, Wu Y (2014) Analysis of solidification cracking susceptibility in side-by-side dual-beam laser welding of aluminum alloys. Int J Adv Manuf Technol 73(1–4): 73–85
4. İpekoğlu G, Erim S, Çam G (2014) Effects of temper condition and post weld heat treatment on the microstructure and mechanical properties of friction stir butt-welded AA7075 Al alloy plates. Int J Adv Manuf Technol 70(1–4):201–213
5. Casalino G, Mortello M (2016) Modeling and experimental analysis of fiber laser offset welding of Al-Ti butt joints. Int J Adv Manuf Technol 83(1–4):89–98
6. Wang Q, Chen H, Zhu Z, Qiu P, Cui Y (2016) A characterization of microstructure and mechanical properties of A6N01S-T5 aluminum alloy hybrid fiber laser-MIG welded joint. Int J Adv Manuf Technol. doi:10.1007/s00170-015-8280-y
7. Ancona A, Lugarà PM, Sorgente D, Tricarico L (2007) Mechanical characterization of CO2 laser beam butt welds of AA5083. J Mater Process Technol 191(1–3):381–384
8. Yang ZB, Tao W, Li LQ, Chen YB, Li FZ, Zhang YL (2012) Double-sided laser beam welded T-joints for aluminum aircraft fuselage panels: process, microstructure, and mechanical properties. Mater Des 33:652–658
9. Gao M, Chen C, Mei S, Wang L, Zeng X (2014) Parameter optimization and mechanism of laser–arc hybrid welding of dissimilar Al alloy and stainless steel. Int J Adv Manuf Technol 74(1–4):199–208
10. Dursun T, Soutis C (2014) Recent developments in advanced aircraft aluminium alloys. Mater Des 56:862–871
11. Molian PA, Srivatsan TS (1990) Weldability of aluminium-lithium alloy 2090 using laser welding. J Mater Sci 25:3347–3358
12. Hou KH, Baeslack WAI (1996) Effect of solute segregation on the weld fusion zone microstructure in CO2 laser beam and gas tungsten arc welds in Al-Li-Cu alloy 2195. J Mater Sci Lett 15(3):208–213
13. Shi Y, Zhong F, Li X, Gong S, Chen L (2007) Effect of laser beam welding on tear toughness of a 1420 aluminum alloy thin sheet. Mater Sci Eng A 465(1–2):153–159
14. Fu B, Qin G, Meng X, Ji Y, Zou Y, Lei Z (2014) Microstructure and mechanical properties of newly developed aluminum–lithium alloy 2A97 welded by fiber laser. Mater Sci Eng A 617:1–11
15. Yan J, Gao M, Li G, Zhang C, Zeng X, Jiang M (2013) Microstructure and mechanical properties of laser-MIG hybrid welding of 1420 Al-Li alloy. Int J Adv Manuf Technol 66(9–12): 1467–1473

16. Karabin LM, Bray GH, Rioja RJ, Venema G, (2012) Al-Li-Cu-Mg-(Ag) Products for lower wing skin applications. Proceedings of the 13th international conference on aluminum alloys (ICAA13). 529–534
17. Zhang X, Yang W, Xiao R (2015) Microstructure and mechanical properties of laser beam welded Al–Li alloy 2060 with Al–Mg filler wire. Mater Des 88:446–450
18. Zhan X, Wang Y, Liu Y, Zhang Q, Li Y, Wei Y (2015) Investigation on parameter optimization for laser welded butt joint of TA15 alloy. Int J Adv Manuf Technol. doi:10.1007/s00170-015-7900-x
19. Li G, Gao M, Chen C, Zhang C, Zeng XY (2014) Characterisation comparison of laser and laser–arc hybrid welding of Invar 36 alloy. Sci Technol Weld Join 19(1):30–37
20. Zhang MJ, Chen GY, Zhang Y, Wu KR (2013) Research on microstructure and mechanical properties of laser keyhole welding–brazing of automotive galvanized steel to aluminum alloy. Mater Des 45:24–30
21. Kong JP, Park TJ, Kim JK, Uhm SH, Woo IS, Lee JS, Park BG et al (2011) Characterization of laser welds in Al–10wt.% Si coated ferritic stainless steel. Mater Des 32(2):917–925
22. Pang S, Chen W, Wang W (2014) A quantitative model of keyhole instability induced porosity in laser welding of titanium alloy. Metall Mater Trans A 45(6):2808–2818